

# Origin of the interlayer exchange coupling in [Co/Pt]/NiO/[Co/Pt] multilayers studied with XAS, XMCD, and micromagnetic modeling

A. Baruth,<sup>1</sup> D. J. Keavney,<sup>2</sup> J. D. Burton,<sup>1</sup> K. Janicka,<sup>1</sup> E. Y. Tsymlal,<sup>1</sup> L. Yuan,<sup>1</sup> S. H. Liou,<sup>1</sup> and S. Adenwalla<sup>1,\*</sup>

<sup>1</sup>*Department of Physics and Astronomy and the Nebraska Center for Materials and Nanoscience, University of Nebraska-Lincoln, Lincoln, Nebraska 68588-0111, USA*

<sup>2</sup>*Advanced Photon Source, Argonne National Lab, Argonne, Illinois 60439, USA*

(Received 1 May 2006; published 17 August 2006)

The origin of the oscillatory interlayer exchange coupling in [Co/Pt]/NiO/[Co/Pt] multilayers is investigated using advanced microscopy and spectroscopy techniques and micromagnetic modeling. X-ray magnetic circular dichroism (XMCD) measurements show the presence of the canting of Ni spins in the NiO film being greater for antiferromagnetically coupled multilayers than for ferromagnetically coupled ones. This behavior is consistent with the model, which assumes a different sign of the exchange coupling at the two interfaces and the antiferromagnetic layer-by-layer coupling in the NiO film. An unexpectedly short attenuation length of 4 Å for secondary electrons in NiO is measured, which has implications for the interpretation of XMCD data. Domain images obtained using XMCD-photoemission electron microscopy at the Co and Ni resonances indicate that the canting of the Ni spins occurs on both a microscopic and macroscopic scale. The average size of the domains is shown to increase with exchange coupling strength. In antiferromagnetically coupled samples, the competition between magnetostatic and interlayer exchange effects gives rise to a region of overlapping domains. The size of this region scales inversely with coupling strength. Finally, the temperature dependence of the interlayer coupling shows both reversible and irreversible effects. The irreversible effects stem from oxidation/reduction reactions at the Co/NiO interface. The reversible effects stem from the temperature dependences of the many factors that play a role in the interlayer coupling and exhibit nonmonotonic temperature dependence.

DOI: [10.1103/PhysRevB.74.054419](https://doi.org/10.1103/PhysRevB.74.054419)

PACS number(s): 75.70.Cn, 75.70.Kw

## I. INTRODUCTION

The investigation of the coupling of ferromagnetic films across nonferromagnetic spacers has resulted in a spectrum of scientific discoveries as well as technologically useful devices.<sup>1</sup> Early investigations into the coupling across metallic spacer layers revealed oscillatory coupling<sup>2</sup> as a function of spacer thickness and the associated phenomenon of the giant magnetoresistive effect.<sup>3</sup> The period of the oscillatory coupling is associated with the spanning vectors of the Fermi surface of the spacer material. For insulating spacers, both theoretical and experimental studies indicate a nonoscillatory monotonic decay of the coupling with increasing spacer thickness.<sup>4,5</sup>

We have previously observed a nonmonotonic oscillatory coupling between two Co/Pt multilayers on either side of a NiO spacer layer.<sup>6,7</sup> In this system, the Co/Pt multilayers have perpendicular easy magnetization axis, while the Ni spins lie in plane. The period of oscillation corresponds to the antiferromagnetic (AFM) ordering period of the NiO, suggesting a correlation of the coupling with the AFM order. The coupling of ferromagnetic (FM) layers across an AFM spacer has been studied by various groups, often in conjunction with the exchange biasing effect. The well-known oscillatory coupling with a 2 monolayer (ML) period seen for Cr (100) spacer layers<sup>8</sup> has been ascribed to a nested feature in the Fermi surface, which also happens to be responsible for the AFM spin density wave. The 2 ML oscillation is not directly attributable to the AFM ordering; in fact, below the Néel temperature of the thin Cr film, the coupling can disappear.<sup>9,10</sup> A model of interlayer exchange coupling (IEC)

through metallic antiferromagnets (the proximity magnetism model<sup>11</sup>) indicates that both the exchange coupling at the interface as well as the propagating spin structure of the AFM spacer have to be taken into account. The spin structure in either the FM and/or the AFM may rotate away from its easy axis at the interface and the anisotropy constants dictate the degree of twisting. In experiments on FM sandwiches coupled across both insulating<sup>12,13</sup> and metallic antiferromagnets,<sup>14</sup> noncollinear coupling has been observed over a substantial range of spacer layer thickness. The presence of atomic layer roughness in the AFM layer leads to a competition between FM coupling between the magnetic layers (favored by an *odd* number of AFM spacer layers) and antiferromagnetic coupling (favored by an *even* number of AFM layers), leading to a compromise that results in a net noncollinear coupling in order to minimize the energy. In these cases, oscillatory coupling as a function of thickness (as would be expected for atomically flat interfaces) is not observed. A recent paper<sup>15</sup> using x-ray magnetic circular dichroism photoelectron microscopy (XMCD-PEEM) shows that in a trilayer with a wedge-shaped FeMn as the antiferromagnetic spacer layer, the top FM layer shows an oscillatory domain pattern with increasing FeMn thickness. These FeMn layers were carefully prepared to be epitaxial, and showed layer-by-layer growth. The lack of oscillatory coupling in previous experiments may stem from the atomic scale roughness of the surfaces. We do not expect that the sputtered NiO layers in our films are atomically flat, yet the oscillatory coupling is clear and unambiguous and has been reproduced for other samples grown in different sputtering chambers with some variation in the exact parameters.<sup>6,7</sup> The

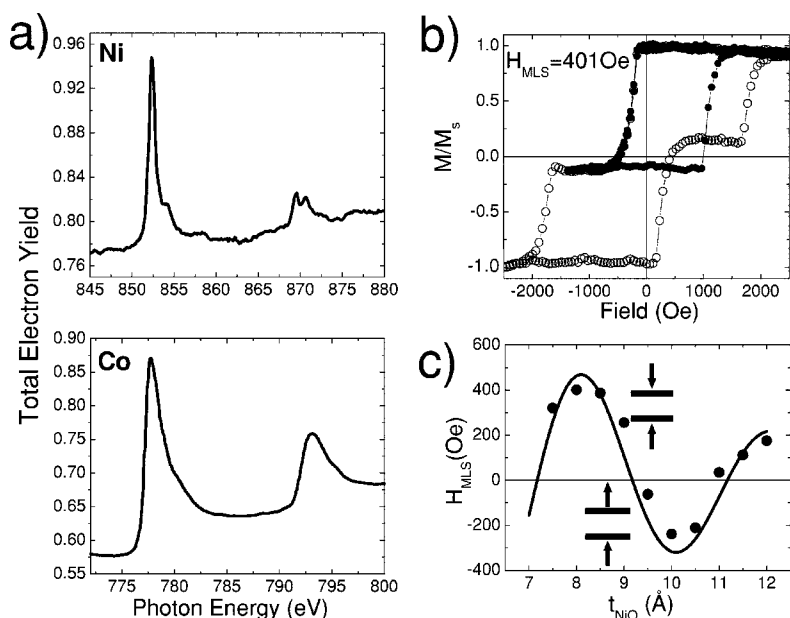


FIG. 1. (a) Room temperature XAS spectra at the Ni and Co  $L_{3,2}$  resonances indicate no evidence of multiplet splitting at the Co  $L_{3,2}$  peaks, as would be expected if CoO were present, and the Ni  $L_2$  peak reveals a doublet splitting, as expected for  $Ni^{2+}$  in NiO. (b) The major and minor hysteresis loops at room temperature for a sample with a NiO thickness of 8 Å, which was measured using polar MOKE. For measurement of the minor loop, a large field was applied to saturate the sample; the field was then decreased until the top Co/Pt multilayer reversed. Then the field was again increased to complete the loop, during this entire loop the bottom Co/Pt multilayer does not switch. (c) The room temperature minor loop shift is a measure of the interlayer exchange coupling, thus the variation in coupling with NiO thickness is given. The coupling oscillates with NiO thickness from antiferromagnetic to ferromagnetic coupling.

perpendicular easy axis of the Co/Pt ferromagnetic layer may play a vital role, since the energy cost associated with noncollinear coupling in this configuration is high.

Theoretical calculations<sup>16</sup> show that the oscillatory coupling can be explained within a model that assumes the exchange interaction at the NiO/Co interfaces and the antiferromagnetic superexchange interaction between Ni moments within the NiO film. The canting of the NiO spins that must occur in order for IEC to take place propagates across the thickness of the NiO, leading to either AFM or FM coupling. In this article we report a study of the canting of NiO spins, the temperature dependence of the coupling, and the behavior of magnetic domains in these oscillatory coupled [Co/Pt]/NiO/[Co/Pt] samples. There is clear evidence for canting of the Ni spins. Detailed examinations of the domain structures in virgin samples confirm that the oscillatory coupling occurs domain by domain. Moreover, the Co spins and the Ni spins cant in coincidence, both macroscopically and microscopically. The temperature dependence of the coupling shows both irreversible changes caused by low-temperature oxidation/reduction reactions at the interface, as well as reversible changes due to the complex interplay of the temperature dependences of the variety of parameters on which the coupling depends.

The manuscript is organized as follows: Sample preparation and experimental measurements are described in Sec. II. Experimental results and discussions involving element specific magnetization of Co and Ni as functions of field as well as x-ray magnetic circular dichroism (XMCD) scans at the Ni photon resonant energy are presented in Sec. III. Section IV presents our results on the domain structure of these multilayers using XMCD-PEEM imaging and MFM. Section V contains the temperature dependence, and a summary and conclusions are presented in Sec. VI.

## II. SAMPLE PREPARATION AND EXPERIMENTAL TECHNIQUES

Two series of samples were prepared as outlined below. The series 1 samples were used only for the total fluores-

cence yield (TFY) measurements. All samples were prepared by dc and rf magnetron sputtering from separate Pt, Co, and NiO targets.

*Series 1:* Samples on glass substrates with varying NiO thickness and Pt capping layers. Deposition rates were 0.96 Å/s, 0.2 Å/s, and 0.19 Å/s, for Pt, Co, and NiO respectively, in 3 mTorr Ar pressure, with base pressure of  $4 \times 10^{-7}$  Torr.

Glass/Pt(100Å)/[Pt(5Å) / Co(4Å)]<sub>3</sub> / NiO( $t_{NiO}$ Å) / [Co(4 Å)/Pt(5 Å)]<sub>3</sub>/Pt(50 Å).  $t_{NiO}$  had values 11 Å and 12 Å.

*Series 2:* Samples on Si substrates with Cu capping layers.

Deposition rates of 0.56 Å/s, 0.26 Å/s, and 0.07 Å/s for Pt, Co, and NiO, respectively, in 2 mTorr Ar pressure with a base pressure of  $3.8 \times 10^{-8}$  Torr.

[A] Samples with varying NiO thickness

Si(111)/Pt(100 Å) / [Pt(6 Å) / Co(4 Å)]<sub>3</sub>/NiO( $t_{NiO}$  Å) × [Co(4 Å)/Pt(6 Å)]<sub>3</sub>/Cu(20 Å).  $t_{NiO}$  ranged from 7.5 Å to 12 Å.

[B] Samples with varying Pt thickness

Si(111)/Pt(100 Å)/[Pt( $t_{Pt}$  Å)/Co(4 Å)]<sub>3</sub>/NiO(8 Å) / [Co(4 × Å)/Pt( $t_{Pt}$  Å)]<sub>3</sub>/Cu(20 Å).  $t_{Pt}$  ranged from 5.1 Å–11.8 Å.

The thickness calibration for series 1 was checked by grazing angle x-ray reflectivity after sample preparation, displaying an accuracy of ~10%. Series 2 was checked using an *in situ* deposition monitor. The sample structure was checked for both series by x-ray diffraction. The Pt layers are polycrystalline, but are highly fcc (111) textured; the Co layers are highly hcp (100) textured, and the NiO layer is highly fcc (111) textured.

Initial magnetic characterization of samples was done *ex situ* using a tabletop magneto-optical Kerr effect (MOKE) setup. A typical room temperature MOKE loop is shown in Fig. 1(b). The upper and lower Co/Pt layers have distinct coercive fields, which we attribute to the differences in the microstructure between the two layers.<sup>17–19</sup> Moreover, the magnetizations of the two layers are unequal—the top multilayer has 1.43 times the out-of-plane magnetization compared to the bottom layer. This ratio of the magnetization

has been confirmed by both alternating gradient field magnetometer (AGFM) and superconducting quantum interference device (SQUID) measurements. Careful studies of the absolute magnetization of Co/Pt multilayers indicate that increasing Pt strain leads to lower than expected values for the saturation magnetization.<sup>20</sup> The intervening NiO spacer layer may change the microstructure of the upper multilayer leading to changes in saturation magnetization, anisotropy, and other magnetic properties.

Evidence of oscillatory IEC at RT for a series of NiO thicknesses was obtained by measurement of the minor loop shift similar to that in Refs. 6 and 7 shown in Fig. 1(c). The samples in this study represent various regions of antiferromagnetic and ferromagnetic coupling based on these MOKE measurements. Temperature-dependent magnetization measurements were made with MOKE using a Janis cryostat with polarization preserving optical windows over a temperature range of 180–470 K.

Element specific characterization was performed using x-ray absorption spectroscopy (XAS) and XMCD at beamline 4-ID-C of the Advanced Photon Source at Argonne National Laboratory. Due to the large separation of the Ni and Co  $L_3$  resonances (778.1 and 852.7 eV, respectively), XAS provides valuable information on the chemical states of the Ni and Co layers separately, while XMCD yields the corresponding magnetization information. The samples were mounted on a liquid He cryostat in a split-coil superconducting magnet with both the field and sample normal parallel to the incident x-ray beam, thus the XMCD data are sensitive only to the normal component of the magnetization. Data was collected in total electron yield (TEY) by monitoring the sample current and in TFY using a Ge detector. One key difference between the two measurements (TEY versus TFY) is the attenuation lengths of the secondary electrons emitted for the TEY measurements versus the fluorescence photons ( $\sim 1$ – $2$  nm vs  $\sim 100$  nm, respectively). TEY measurements are therefore more heavily weighted by the upper layers and accounting for this attenuation plays an important role in the interpretation of the TEY data obtained.

Element-specific magnetic domain images were obtained using XMCD-PEEM at the same beamline. XMCD-PEEM provides a map of the absorption contrast with spatial resolution of  $\sim 100$  nm, thus high-resolution images of surfaces and interfaces with elemental and magnetic contrast can be obtained by tuning to the appropriate incident energy. In this part of the experiment, as-grown (virgin) samples with varying NiO and Pt thicknesses were mounted in the XMCD-PEEM with an incidence angle of  $25^\circ$  above the surface of the sample. In this orientation, the resulting domain images are sensitive to both in-plane and out-of-plane magnetization components. However, both previous<sup>7</sup> and current magnetic force microscopy (MFM) domain images shown in Sec. V clearly indicate that the magnetic domains are oriented perpendicular to the sample plane.

The MFM images were measured in tapping/lift mode at a lift height of 5 nm under ambient conditions. The MFM tip consists of a 30 nm thick CoPt film with a coercivity of  $\sim 15$  kOe (Ref. 21) coated onto a soft cantilever. The MFM tip is magnetized along a direction perpendicular to the sample surface, pointing downwards.

### III. XAS AND XMCD MEASUREMENTS AT Co AND Ni RESONANT ENERGIES

#### A. XAS

In Fig. 1(a), we show room temperature XAS energy scans with a resolution of 0.25 eV through the Ni and Co  $L_{3,2}$  resonances. These scans indicate no evidence of multiplet splitting at the Co  $L_{3,2}$  peaks, as would be expected if CoO were present. Comparison of the XAS signature to that of a pure Co film (evaporated *in situ* in UHV) reveal that the  $L_3$  line shape is identical and there are no features pre- or post-edge as there would be with an oxide. The Ni  $L_2$  peak reveals a doublet splitting, as expected for  $\text{Ni}^{2+}$  in NiO. This stands in sharp contrast to previous spectroscopic studies of the Co/NiO interface, which indicate a region of CoO and Ni formation in molecular beam epitaxy (MBE) grown interfaces.<sup>22,23</sup> We do not see, at similar energy resolution, any formation of a mixed Co-Ni-O compound at the interface region, as evidenced by the lack of multiplet splitting in the Co XAS scan about the  $L_2$  or  $L_3$  edges. Previous measurements of metal-oxide interfaces consisted of MgO/NiO(10 Å)/Co(10 Å)/Ru, whereas our samples contain considerably more material above the Co/NiO interface, an effect that could lead to considerable attenuation of the secondary electrons. In Ref. 23, the oxidation of Co was limited to about 2 Å at the Co/NiO interface. In order to calculate the fraction of the Co signal that arises from this thin layer at the interface, we follow the procedure outlined by O'Brien and Tonner,<sup>24</sup> where the contribution from a single Co layer of thickness  $dz$  is

$$dN_{\text{Co}} = I_o m_{\text{Co}} \mu_{\text{Co}} G_{\text{Co}} e^{-z(\mu_{\text{Co}} + 1/\lambda_{\text{Co}})} dz, \quad (1)$$

where  $I_o$  is the incident photon intensity,  $m_{\text{Co}}$  is the magnetization contribution from the Co layer,  $\mu_{\text{Co}}$  is the photon attenuation through the Co,  $G_{\text{Co}}$  is the number of created electrons due to the incident photon, and  $\lambda_{\text{Co}}$  is the electron attenuation through the Co layer. Integration of  $dN_{\text{Co}}$  over the thickness of a single Co monolayer gives the TEY contribution from that layer

$$N_{\text{Co}} = I_o \frac{m_{\text{Co}} G_{\text{Co}}}{1 + \frac{1}{\mu_{\text{Co}} \lambda_{\text{Co}}}} [1 - e^{-t_{\text{Co}}(\mu_{\text{Co}} + 1/\lambda_{\text{Co}})}]. \quad (2)$$

Due to photon and electron attenuation from the Pt, Cu, and NiO layers, there will be a different TEY contribution from each of the six Co layers based on the layers that cover it. There are four possible attenuation contributions,

$$A = t_{\text{Co}} \left( \mu_{\text{Co}} + \frac{1}{\lambda_{\text{Co}}} \right),$$

$$B = t_{\text{Pt}} \left( \mu_{\text{Pt}} + \frac{1}{\lambda_{\text{Pt}}} \right),$$

$$C = t_{\text{Cu}} \left( \mu_{\text{Cu}} + \frac{1}{\lambda_{\text{Cu}}} \right),$$

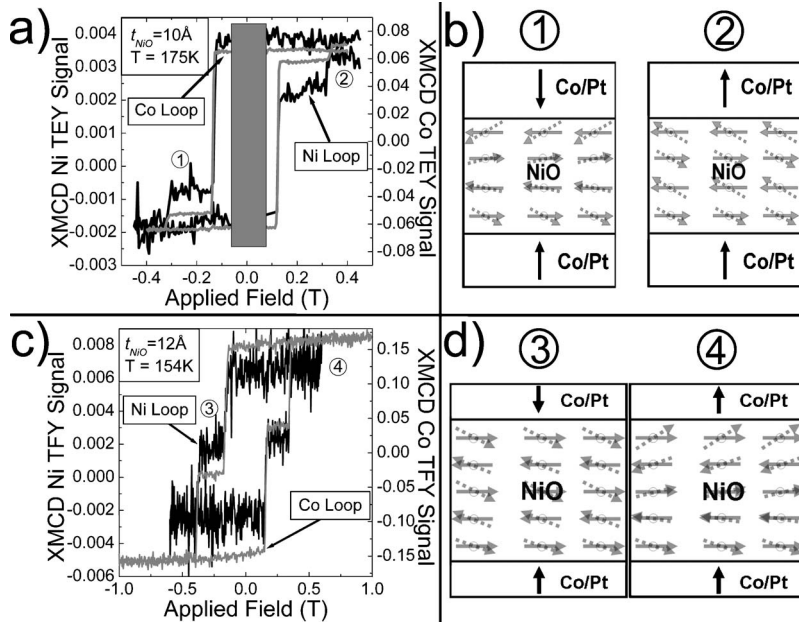


FIG. 2. (a) Element-specific magnetization loops for Co and Ni taken with x-ray magnetic circular dichroism in total electron yield mode at 175 K on a ferromagnetically coupled, series 2 sample with a 10 Å thickness of NiO. (b) Possible NiO spin configuration for a ferromagnetically coupled sample in the *antiferromagnetic* state (①) and *ferromagnetic* state (②), leading to the net Ni out-of-plane magnetization presented in (a) (See Sec. III C in the text for details on exchange coupling at the Co/NiO interface.) (c) Element-specific magnetization loops for Co and Ni taken with x-ray magnetic circular dichroism in total fluorescence yield mode at 154 K on an antiferromagnetically coupled, series 1 sample with a 12 Å thickness of NiO. (d) Possible NiO spin configuration for an antiferromagnetically coupled sample in the *antiferromagnetic* state (③) and *ferromagnetic* state (④), leading to the net Ni out-of-plane magnetization presented in (c).

$$D = t_{\text{NiO}} \left( \mu_{\text{NiO}} + \frac{1}{\lambda_{\text{NiO}}} \right). \quad (3)$$

Using these definitions, the Co layers which lie in intimate contact with the NiO will have contributions

$$I_{\text{top}} = I_o \frac{m_{\text{Co(top)}} G_{\text{Co}}}{1 + \frac{1}{\mu_{\text{Co}} \lambda_{\text{Co}}}} (1 - e^{-A})(e^{-4A})(e^{-3B})(e^{-C}) \quad (4)$$

and

$$I_{\text{bottom}} = I_o \frac{m_{\text{Co(bottom)}} G_{\text{Co}}}{1 + \frac{1}{\mu_{\text{Co}} \lambda_{\text{Co}}}} (1 - e^{-A})(e^{-6A})(e^{-3B})(e^{-C})(e^{-D}). \quad (5)$$

Doing a similar treatment for the remaining layers of Co allows a ratio of these two sandwiched layers to the rest of the Co to be calculated. For this calculation, we choose  $\lambda_{\text{Co}} = 25$  Å (Ref. 25),  $t_{\text{Co}} = 2$  Å, and  $\mu_{\text{Co}} = 1/180$  Å (Ref. 26). The photon attenuation through Pt and NiO is nearly negligible where  $\mu_{\text{Pt}}$  is 1/620 Å and  $\mu_{\text{NiO}}$  is 1/4846 Å (Ref. 26). The electron attenuation through Pt has not been studied, but using the universal energy curve,<sup>26,27</sup> we assume an attenuation length of 60 Å. A secondary electron mean free path of around 4 Å is used for the NiO; this will be shown to be experimentally accurate later in this text. With these values, the 2 Å layers of Co that are in intimate contact with the NiO make up 13.6% of the total Co contribution in the 8 Å sample, where this percentage is highly sensitive to the electron attenuation through the NiO and Pt. Even though the multiplet splitting would occur in only 13.6% of the contributing Co, the expected multiplet features are sufficiently far from the main absorption peak and they would be easily visible. In particular, the absence of pre-edge intensity strongly argues against a significant amount of nonmetallic

Co. Hence at room temperature and below we assume that there are negligible amounts of CoO at the Co/NiO interface.

## B. XMCD hysteresis loops and electron attenuation length in NiO

In Figs. 2(a) and 2(c) we show the element-specific magnetization loops for Co and Ni obtained by tuning to the appropriate  $L_3$  resonance and measuring the field-dependent XMCD in both TEY and TFY modes. In the TEY data, the lower field data is not shown due to artifacts that result from the varying field and photoelectron trajectories. The hysteresis loops were measured for strongly and weakly AFM and FM coupled samples, above and below the blocking temperature; shown are a FM [Fig. 2(a)] and an AFM [Fig. 2(c)] coupled sample, taken at 175 K and 154 K, respectively. The x-ray beam is incident normal to the sample plane; in this geometry, we are sensitive only to the out-of-plane component of the magnetization. The square shapes of all three loops are suggestive of the expected out-of-plane easy axis of the Co. The exchange bias effect is clearly visible as a net shift of the lower temperature loops [shown in Figs. 2(a) and 2(c)], an effect which disappears above the blocking temperature of 250 K for these samples. Similar effects have been seen with MOKE and SQUID for the  $[\text{Pt}/\text{Co}]_n/\text{NiO}/[\text{Co}/\text{Pt}]_n$  system<sup>6,7,28</sup> and show the coexistence of exchange coupling and exchange bias at temperatures below the blocking temperature. A very large difference in the signal from the top and bottom Co/Pt multilayers was observed for the TEY data (much larger than that seen in TFY or MOKE data), clearly due to the attenuation of the secondary electrons from the bottom Co/Pt layer through the very thin NiO layer and the top Co/Pt layer (see study below). MOKE, SQUID, and AGFM measurements on a variety of samples give a ratio of 1.43 for the magnetization of the top and bottom Co/Pt multilayers. This ratio was observed to be the similar for all samples studied (8, 9.5, 11,

and 12 Å) over a wide range of temperatures (180 K–300 K).

Both TEY and TFY data indicate that the Ni magnetization, although much smaller than the Co magnetization, as evidenced by the poorer signal-to-noise ratio, follows in lockstep with the Co magnetization. We also note [Fig. 1(a)] that the Ni XMCD line shape in all these samples exhibits a multiplet splitting indicative of a Ni<sup>2+</sup> state, which shows that this XMCD signal originates in the NiO layer, and not a minority metallic phase. This implies that the Ni spins in the intervening insulating AFM NiO layer cant up and down out of plane in concert with the neighboring Co layers [Fig. 2(b) and 2(d)]. In the AFM coupled state [the plateau region at low field, indicated by ① and ③ in Figs. 2(a) and 2(c), respectively] the magnitude of the net Ni magnetization is minimized. The resultant magnetization is not zero due to a range of canting angles from the top to bottom of the NiO layer in addition to attenuation effects through the NiO; this canting phenomenon is fully discussed in the next section. In order to study this canting, which is predicted<sup>16</sup> to play a key role in the coupling, we pose two questions: do both interfacial layers of Ni spins (i.e., the upper and lower) cant an equal amount, and how is this canting propagated through the bulk? In order to answer these questions, it is necessary to address the attenuation of the TEY signal through the NiO layer.

For the Co loops, the TEY signal arising from the lower multilayer is considerably smaller than that from the upper one. This is also seen in the Ni loops, where the signal arising from the lower NiO layer is smaller than from the upper layer (the Ni layers cant at different fields, given by the coercivities of the neighboring Co/Pt multilayer). The dramatic attenuation of the electron signal arising from only ~1 nm of NiO is somewhat surprising. Previous estimates of the attenuation length of NiO range from 2–3 nm.<sup>23</sup> However, this attenuation length implies an almost negligible attenuation for our very thin NiO spacer layers, certainly much smaller than the almost tenfold reduction we see. No published measurements of the electron attenuation length in NiO exist. Therefore, in order to obtain a direct measurement for comparison with our XMCD data, a calibrated wedge-shaped NiO sample with a Co/Pt underlayer and a Cu cap was made. Low-angle x-ray reflectivity measurements were used to obtain a functional model for the thickness of a NiO wedge grown under identical conditions for a longer time. Figure 3 inset shows the position-dependent thickness of the thinner NiO wedge used, obtained by scaling down thicknesses with time. The two edges of the wedge were sharply masked to allow for cross calibration of the position. This calibrated sample was loaded into the 4-ID-C beamline at the Advanced Photon Source. The room temperature TEY signal at the Co resonance arising from the lower Co layer was recorded as a function of sample position and correlated with NiO thickness. The integrated Co XAS signal is shown as a function of NiO thickness in Fig. 3. The resulting exponential fit indicates an attenuation length of 4 Å in NiO, much smaller than previous estimates of about 30 Å.<sup>23</sup> We have made the following assumptions: (i) that the photon absorption in the wedge-shaped NiO is negligible, a reasonable assumption since the measurements are made at the Co *L*<sub>3</sub>

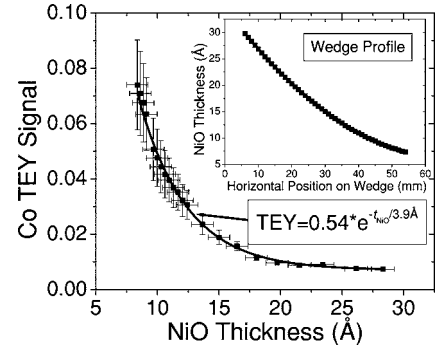


FIG. 3. Measurement of the secondary electron attenuation length in NiO. The total electron yield signal arising from the Co *L*<sub>3</sub> resonance on a [Co/Pt]<sub>3</sub>/NiO/Cu sample is measured at room temperature, where the NiO thickness varies with position. The exponential fit indicates an attenuation length for secondary electrons in NiO of 3.9 Å. The inset shows the profile of the NiO wedge, characterized with low-angle x-ray reflectivity.

resonance, well below the Ni resonance, and (ii) that there is a negligible incident photon energy dependence on this attenuation length between the Co and Ni resonances. Although the attenuation length of secondary electrons is energy specific, the TEY consists primarily of secondaries, with a range of energies below ~10 eV. The difference in the secondary electron energy distribution and hence the attenuation lengths at the Co and Ni resonance edges (778.1 eV and 852.7 eV respectively) is therefore very small. Thus we use this value of 4 Å in the discussion of what follows. A similarly short attenuation length of 4–5 Å was measured<sup>29</sup> for polarized low-energy secondary electrons in NiO, excited by an 800 eV electron beam. Assuming that the attenuation is independent of the spin polarization, the result in Ref. 29 provides strong support for our result.

Predictions of the ratio between the top and bottom Co/Pt multilayer TEY signal can be made based on the secondary electron attenuation measurements in NiO. Following from our previous results for the XAS signal from the sandwiching Co layers, we can also use this approach to determine the expected magnetization ratios from the top to bottom Co/Pt multilayers. Using previous definitions in Eq. (3), the contribution from the top three Co layers is

$$I_{n=1,2,3} = I_o \frac{m_{\text{Co(top)}} G_{\text{Co}}}{1 + \frac{1}{\mu_{\text{Co}} \lambda_{\text{Co}}}} (1 - e^{-nA})(e^{-(n-1)A})(e^{-nB})(e^{-nC}) \quad (6)$$

and the bottom layers is

$$I_{n=4,5,6} = I_o \frac{m_{\text{Co(bottom)}} G_{\text{Co}}}{1 + \frac{1}{\mu_{\text{Co}} \lambda_{\text{Co}}}} (1 - e^{-nA})(e^{-(n-1)A})(e^{-(n-1)B})(e^{-nC}) \times (e^{-D}). \quad (7)$$

Thus, the TEY ratio of top to bottom is then

TABLE I. Comparison of expected and experimental TEY ratios from the upper and lower Co/Pt multilayers. For details see text.

Thickness of NiO (Å)	Calculated TEY Ratio	Experimental TEY Ratio
8	22.7	9.5
10	37.6	14.6
11	48.2	15.3
12	61.9	17.0

$$\text{Ratio} = \frac{m_{\text{Co(top)}}(l_1 + l_2 + l_3)}{m_{\text{Co(bottom)}}(l_4 + l_5 + l_6)} = \frac{m_{\text{Co(top)}}}{m_{\text{Co(bottom)}}} e^{3A} e^{2B} e^C. \quad (8)$$

As discussed, MOKE measurements on these samples give a ratio of the Co magnetization from top to bottom to be roughly 1.43 for all thickness of NiO over this temperature range. Thus, the TEY ratio is given by

$$\text{Ratio} = 1.43 e^{3A} e^{2B} e^C, \quad (9)$$

With the same values we used previously we obtain the calculated TEY ratios. Comparison of these values to the experimental ratios is given in Table I.

A large discrepancy between the calculated and observed TEY ratios is seen. Alternatively, if we assume the experimental TEY ratio is correct, we obtain a  $\lambda_{\text{NiO}}$  of nearly 7 Å, larger than the 4 Å we have measured. This value is still much smaller than previous estimates, but it is significantly different than our anticipated 4 Å value. As a similar wedge sample was carefully calibrated using low-angle x-ray reflectivity, we expected an error of less than 10%. There are several possible explanations for this discrepancy between the experimental and calculated values. (i) Inaccurate absolute thickness calibrations in our series 2 samples. The sample thicknesses were characterized by *in situ* deposition monitoring, which is less accurate than the x-ray reflectivity and not necessarily consistent over long periods of time following a calibration. (ii) Nonuniform deposition rates, causing an error in the NiO thickness for the thin wedge-shaped NiO sample on which the experiment was performed. (iii) The uncertainties in the other constants, such as the attenuation of the secondary electrons through Co and Pt; varying these parameters will close the gap between the experimental and calculated values. Regardless of these variations, a very short attenuation length is observed for NiO and must be taken into account in this study.

### C. Ni canting

We probed the relationship between the canting angles of the Ni moments and the strength of the IEC by measuring the XMCD signal of the Ni layer at normal incidence for a range of samples with varying coupling strengths. The normal incidence XMCD scans were performed about the  $L_3$  edge of Ni, at 852.7 eV (Fig. 4). All measurements were made at high enough fields such that the Co magnetization was saturated, i.e., the Co/Pt layers were in a *ferromagnetic* state (Fig. 2, points ②, and ④ and were taken at 175 K. Based on

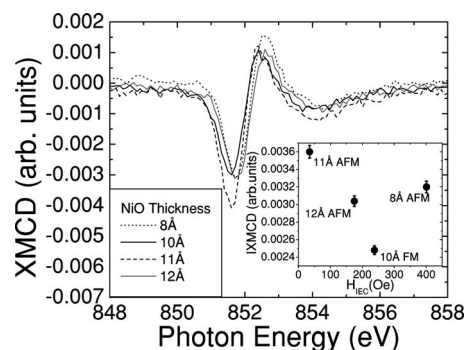


FIG. 4. XMCD signal at the Ni  $L_3$  resonance for the 8, 10, 11, and 12 Å samples, taken at 175 K. The integral over this signal gives a measure of the net out-of-plane magnetization in the antiferromagnetic NiO. Inset: The magnitude of the integral over the dichroism signal vs the magnitude of the coupling strength for the given sample. A larger out-of-plane signal arises for the AFM coupled samples when compared to the FM coupled sample.

the model proposed by Zhuravlev *et al.*<sup>16</sup> we expect the Ni moments within the NiO structure to cant out of the (111) plane with the resultant canting angle arising from the competition between the coupling across the two Co/NiO interfaces, the AFM exchange in NiO and the out-of-plane  $K_1$  anisotropy constant of the NiO. The antiferromagnetic order in NiO (111) consists of spins oriented along the three  $\langle 11\bar{2} \rangle$  directions, which lie in the (111) plane.<sup>30</sup> The ferromagnetic (111) sheets stack antiferromagnetically in the  $\langle 111 \rangle$  direction. Due to the lack of in-plane anisotropy, all possible spin orientations exist within the plane. The exchange interaction with the adjacent Co causes a canting of the spins, forming a cone of constant half-angle  $\theta$  and the NiO XMCD signal is proportional to  $\cos(\theta)$ . The integrated XMCD (IXMCD) signal shown in the Fig. 4 inset is a measure of the net out-of-plane signal from these Ni spins and is found by integration over the dichroism signal normalized to the total XAS signal.

One complication arising from the short attenuation length of secondary electrons in NiO is that the signal in Fig. 4 is heavily weighted in favor of the upper NiO layers. Even for the thinnest NiO sample (8 Å), the lower NiO interface contributes only about 10% to the total signal. This IXMCD signal is then weighted by the attenuation effects from the NiO layer. For example, the bottom layer for the 12 Å sample will contribute less to the total Ni magnetization than it will for the 8 Å sample. It should be noted that these XMCD measurements alone do not reveal the actual layer-by-layer configuration of the spins, but are able to measure the overall canting contribution to the out-of-plane magnetization. Figure 4 shows the measure of this out-of-plane contribution as a function of the magnitude of the coupling strength. The data show that the AFM coupled samples have a larger out-of-plane net Ni signal than that of the FM coupled samples.

In order to explain the experimental data, we use a model proposed by Zhuravlev *et al.*<sup>16</sup> who attributed the IEC to the exchange interaction at both Co/NiO interfaces and the antiferromagnetic superexchange interaction within the NiO film. In that work the coupling at both the top and the bottom

Co/NiO interfaces was assumed to be FM and of the same magnitude. It was found that AFM (FM) IEC occurred for an even (odd) number of NiO MLs, hence leading to the experimentally observed oscillatory coupling. In the saturated state where both Co/Pt layers are aligned parallel (Fig. 2, points ②, and ④), such a consideration leads to a large out-of-plane signal for FM coupled samples, with one uncompensated layer, and a much smaller signal for AFM coupled samples. If, however, the interfacial exchange coupling has opposite signs at the top and bottom interfaces the model predicts the opposite case, namely, that an odd (even) number of NiO MLs leads to AFM (FM) IEC. Based on the conclusions of Fig. 4, namely that the AFM coupled samples have a larger out-of-plane signal than the FM coupled samples, we believe this is the case for our work.

If the couplings at the top and bottom interfaces have differing magnitudes (as well as signs), the Ni spins near the stronger coupled interface will have a larger canting angle leading to an asymmetric spin configuration across the NiO. This asymmetry in the NiO canting is figuratively shown in Figs. 2(b) and 2(d), where the net Ni magnetization found in the hysteresis loops in Figs. 2(a) and 2(c) is due to this asymmetry. From hysteresis loops taken below the blocking temperature, we find that the exchange bias field acting on the top Co/Pt multilayer is approximately twice that for the bottom film, so a similar consideration was taken for the interfacial exchange coupling. Also, since the net Ni magnetization is aligned parallel to the Co/Pt magnetization [since the XMCD hysteresis loops for Co and Ni match in Figs. 2(a) and 2(c)], we deduce that the stronger interface coupling at the top is FM in nature, as we are most sensitive to the topmost layer due to attenuation. These considerations explain the data found in Fig. 4.

A possible mechanism for the different exchange coupling at the two interfaces could be that the termination of NiO at the two interfaces is different—for example, Ni terminated interface at the top and O terminated at the bottom. The direct Ni-Co exchange interaction at the top would most likely lead to FM coupling. At the bottom interface, however, coupling between Ni and Co spins would be mediated by the superexchange interaction through the O terminated interface and would lead to an AFM coupling, as it does in NiO itself. Since the two couplings have different physical origins, it is reasonable to assume that the two will have different magnitudes, as is reflected in the different exchange bias for the top and bottom Co/Pt multilayers. The results of Fig. 4 should be regarded as indirect evidence for this mechanism, and further experimental investigations are needed to confirm our assumptions.

#### IV. DOMAIN STRUCTURES USING XMCD-PEEM AND MFM

All domain imaging was performed on virgin samples, in zero applied field and at room temperature. Both XMCD-PEEM and MFM were used, providing complementary data.

##### A. Coincidence of domains in NiO and Co: XMCD-PEEM measurements

Magnetic domain images were taken using XMCD-PEEM on a virgin, as-grown sample, with  $t_{\text{NiO}}=8$  Å, corresponding

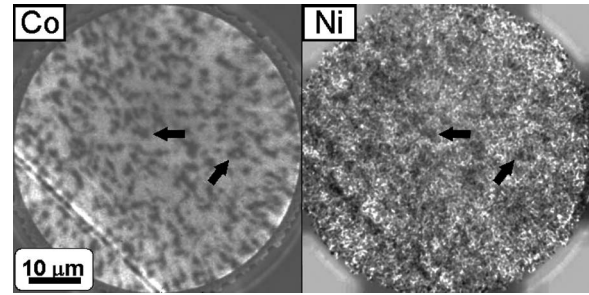


FIG. 5. X-ray magnetic circular dichroism-photoemission electron microscopy images taken at room temperature at the Co and Ni  $L_3$  resonances on a virgin, antiferromagnetically coupled, 8 Å sample from series 2. This technique images ferromagnetic domains in both the top Co and buried NiO layers. There is exact coincidence in the domain structure of the Co and NiO. Arrows indicate the position of coincident domains.

to the strongest AFM coupling in the series 2 sample set. In Fig. 5, we show images of the difference obtained for right and left circularly polarized x-rays taken at the (a) Co and (b) Ni  $L_3$  edges. In these perpendicularly oriented films, the contrast in the XMCD-PEEM images corresponds to up (light) and down (dark) domains. Due to the strong attenuation of secondary electrons originating from the bottom Co/Pt layer, we primarily see the contribution from the top Co/Pt multilayer. The image taken at the Ni resonance, shown in Fig. 5(b) shows an identical domain configuration, with a very weak contrast. We emphasize that these images are XMCD images, hence the domains seen in NiO correspond to a net magnetization of the NiO perpendicular to the film plane (as discussed earlier, all possible spin orientations exist within the plane), and not antiferromagnetic domains as would be seen by magnetic linear dichroism. The domain images are exactly coincident: arrows indicate the location of strikingly similar features. The domain-by-domain correspondence implies that the Ni spins cant in coincidence with the Co magnetization at a microscopic level, and rules out a minority ferromagnetic Ni phase as the explanation for the Ni moment seen by XMCD. Hence the Ni and Co spins follow in lockstep throughout the sample on both a macroscopic (as seen with element specific magnetization curves) and a microscopic level.

##### B. Variation in domain size with coupling strength: XMCD PEEM images at Co $L_3$ edge

XMCD-PEEM images were taken at the Co  $L_3$  resonance for a variety of series 2 samples with varying coupling strength, and are shown in Fig. 6. Previous measurements<sup>7</sup> indicate a variation in coupling strength as the Pt thickness was varied. To generalize our result, we account for changes in IEC due to both Pt and NiO thickness variations and investigate the domain size as a function of coupling strength. Once again, only the contribution from the top Co/Pt multilayer is visible due to attenuation. The domain images indicate that the weaker coupled samples form very small domains that surround the larger domains that form for all samples. These smaller domains developed as wispy do-

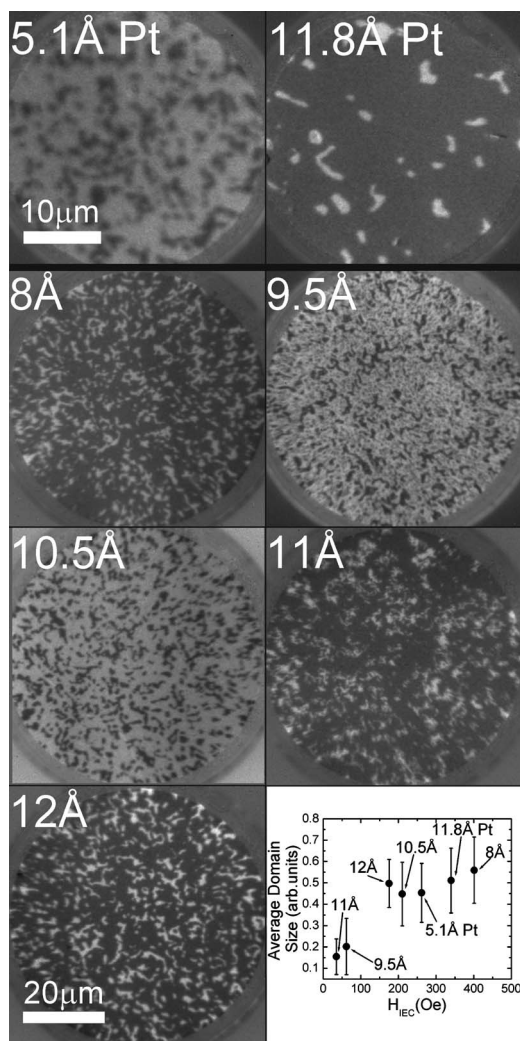


FIG. 6. XMCD-PEEM images taken at room temperature at the Co  $L_3$  resonance on virgin samples representing various NiO and Pt thicknesses. Due to attenuation this measurement is only sensitive to the top Co layers. The top two images represent two Pt thicknesses (5.1 and 11.8 Å), where the NiO thickness was set to 8 Å. The lower five images represent varying NiO thicknesses (8, 9.5, 10.5, 11, and 12 Å). The plot shows the average domain size of these samples as a function of their coupling strength. The average domain size tends to increase with increasing coupling strength, no matter how this variation in coupling is attained (varying NiO or Pt thickness).

mains in the 11 Å and small speckle domains in the 9.5 Å, which represent the weakest coupling. Using IMAGEJ, a public domain Java image processing program inspired by NIH IMAGE for the Macintosh,<sup>31</sup> the average domain size was determined for each sample. IMAGEJ was designed with an open architecture that provides extensibility via Java plug-ins. Using one such Java plug-in, we were able to determine the average size of each domain. This particular plug-in allows the user to define a boundary (domain edge) and then mask all possible domains. The areas of these masks are separated into 256 bins and are then plotted as a histogram. From this histogram an average size can be determined. A direct correlation between the magnitude of the coupling

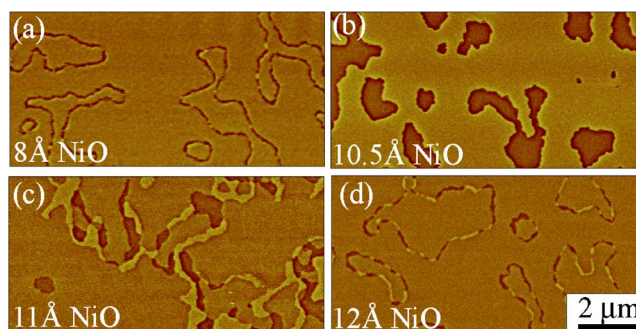


FIG. 7. (Color online) Room temperature MFM images of samples with 8, 10.5, 11, and 12 Å NiO thicknesses. The 8 and 12 Å samples are antiferromagnetically coupled, up and down domains disappear and only a domain overlap region is observed. The 10.5 Å sample is ferromagnetically coupled and only up and down domains are observed. The 11 Å is very weakly coupled (slightly antiferromagnetic). The domain overlap that occurs in the antiferromagnetically coupled samples grows with decreasing coupling strength, where the 8 Å is the strongest and 12 Å is the most weakly coupled sample. The orientation flips from up to down along the overlap to minimize magnetostatic energy.

strength and domain size was established, where the error bars give a measure of the spread in domain size (Fig. 6). Note that this effect is independent of both the sign of the coupling (whether FM or AFM) and the method used to vary the coupling strength (i.e., changing either the NiO or Pt thickness). The nonmonotonic dependence on the thickness of the intervening NiO layer provides a strong argument against purely magnetostatic effects. Clearly, the strength of the interlayer coupling plays a major role in determining the domain size in these coupled samples.

Qualitatively, we may consider the IEC as playing the role of an effective anisotropy. Then, a decrease in the coupling lowers the energy cost for domain formation leading to the formation of smaller domains for the weakly coupled samples to minimize the magnetostatic self-energy.

### C. MFM images of varying NiO thickness

MFM images, in contrast to the XMCD-PEEM images above, see both the upper and lower Co/Pt multilayers. In Fig. 7 the light-colored areas correspond to a magnetization pointing up. For AFM coupled samples, the only contrast appears in the domain wall regions, as can be seen in Figs. 7(a) and 7(d), since the Co/Pt layers order antiferromagnetically domain-by domain.<sup>7</sup> For FM coupled samples [Fig. 7(b)], clear up and down domains are visible. An intriguing feature appears within the domain wall of AFM coupled samples: small FM domains are formed within the domain wall by a slight relative shift of the domains in the upper and lower multilayer. This is most clearly visible in the 12 Å NiO sample. Similar effects have been seen in an AFM coupled sample of Co/Pt separated by Ru.<sup>32</sup> The weaker AFM coupling in the 12 Å sample (as compared to the 8 Å sample) makes domain overlap energetically favorable in order to reduce the magnetostatic energy at the expense of the IEC. Also clearly visible in Fig. 7(d) are “stripes” in the FM

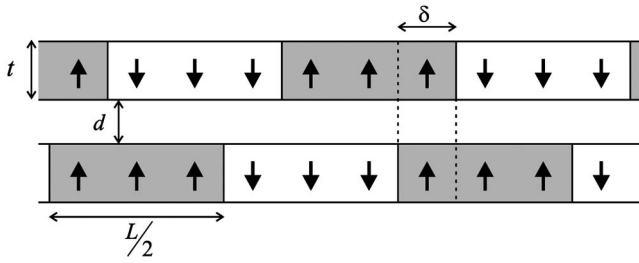


FIG. 8. The model domain structure for the two Co/Pt multilayers. The view is in the plane of the film along the stripe domains. The dimensions are defined in the text.

domain overlap region corresponding to opposite net magnetizations in the domain wall. The dipolar energy within the domain wall region is reduced by having the orientation of the FM region reverse periodically along this overlap of the upper and lower domains. This process leads to the formation of both up and down FM domains that form periodically throughout this overlap. The region of overlap of the upper and lower domain structure increases dramatically for the weakest AFM coupled sample (11 Å), due to a significant decrease in AFM exchange energy. In this sample, with very weak interlayer exchange energy, magnetostatic effects play a large role, leading to domain overlaps that are a significant fraction of the domain size.

To model this behavior, we developed a simple model of two identical magnetic layers of thickness  $t$  separated by distance  $d$ , as shown in Fig. 8. The magnetization in each layer is a periodic system of stripe domains with magnetization directed perpendicularly to the plane. There are two domains of equal size within one period  $L$ . The magnetization changes abruptly by  $180^\circ$  from one stripe domain to the next, i.e., the variation of the magnetization within the domain wall is neglected. We assume that the domain patterns in the two layers are displaced with respect to each other by  $\delta$ . The magnetostatic energy is calculated using the method described in Refs. 33 and 34.

Here we consider only the AFM IEC, since in FM coupled samples the FM configuration corresponds to a minimization of both the exchange coupling and the dipolar energy (since the magnetization of the two films is constrained to remain perpendicular to the film plane). In the calculations we assume a  $[\text{Co/Pt}]_3$  thickness of  $t=3$  nm, the thickness of NiO  $d=1$  nm, and the stripe width  $L=3.22$   $\mu\text{m}$  corresponding to the equilibrium domain size according to XMCD-PEEM measurements. The energy of the IEC through the spacer is given by  $E_{\text{IEC}}=4J_{\text{IEC}}\delta/Lt$ , where  $J_{\text{IEC}}$  is the coupling constant.

The total energy as a function of  $\delta$  for an AFM exchange coupling  $J_{\text{IEC}}=0.1, 0.033,$  and  $0.015$   $\text{erg}/\text{cm}^2$  is displayed in the Fig. 9 inset, where the latter two values correspond to the 8 Å and 12 Å samples, respectively. There is a small but nonzero value of  $\delta$  for which the energy is minimal, so the magnetizations of the two layers are mostly antiparallel except for a small overlapping region as observed in Fig. 7. This overlap arises due to the competition between the magnetostatic interaction and the IEC: the magnetostatic interaction favors parallel alignment whereas the exchange interac-

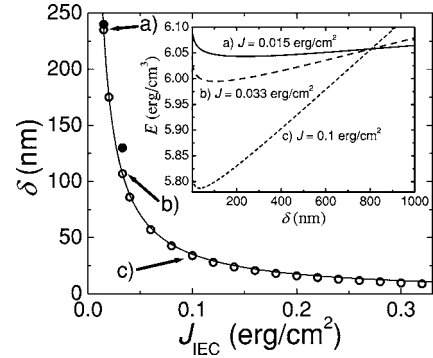


FIG. 9. The dependence of the equilibrium domain overlap  $\delta$  on the interlayer exchange coupling  $J_{\text{IEC}}$ . The open circles are results of the numerical calculation for periodic stripe domains, and the curve calculated directly from Eq. (11). Arrows indicate specific values for  $J_{\text{IEC}}$  as defined in the inset. The closed circles show the measured  $\delta$  values for the 12 and 8 Å samples, as defined in the text. Inset: The variation in the total energy versus the overlap  $\delta$  for three  $J_{\text{IEC}}$  values (a) 0.015, (b) 0.033, and (c) 0.1  $\text{erg}/\text{cm}^2$ , where (a) and (b) correspond to the coupling for the 12 and 8 Å samples, respectively.

tion prefers antiparallel alignment of the domains. On average, the IEC dominates the magnetostatic interaction and if the two were homogeneous over the surface the domains would align perfectly antiparallel with no overlap. However, the magnetostatic coupling is strongly inhomogeneous over the surface due to the stray fields localized in the vicinity of the domain walls. That makes it energetically favorable to produce a small shift  $\delta$  between the antiparallel aligned domains to reduce the magnetostatic energy.<sup>32</sup> With increasing the IEC constant the value of  $\delta$  decreases with  $J_{\text{IEC}}$ , as is seen from the results of calculation shown in Fig. 9 by solid circles.

It can be shown from a simple analytic calculation that the variation of  $\delta$  is inversely proportional to  $J_{\text{IEC}}$ . In the limit of large  $L$ , the perpendicular component of the field produced by the lower Co/Pt multilayer with a domain wall at  $x=0$  can be written as

$$H_z(x, z) = -4M \left[ \arctan\left(\frac{z-t}{x}\right) - \arctan\left(\frac{z}{x}\right) \right], \quad (10)$$

where  $z$  is the distance above the film. This field acts on the upper Co/Pt multilayer with a domain wall at  $x=\delta$ . For  $\delta \gg d$ , as appears to be the case in Fig. 7, the magnetostatic energy of the interaction of these two domain walls is proportional to  $\ln(1/\delta)$  and the competition with the interlayer exchange interaction leads to a finite overlap given by

$$\delta = \frac{8M^2 t^2}{J_{\text{IEC}}}. \quad (11)$$

The variation of  $\delta$  calculated using Eq. (11) is plotted in Fig. 9 by the solid line showing an excellent agreement with the results of the numerical calculations for the periodic system of stripe domains.

Now we compare the results of the domain width calculations to the experimental results. For the weakly coupled

sample (with 12 Å of NiO) the strength of the IEC is 0.015 erg/cm<sup>2</sup>, Eq. (11) yields a domain wall width of 235 nm. For the stronger coupled 8 Å sample, corresponding to an interlayer coupling strength of 0.033 erg/cm<sup>2</sup>, Eq. (11) calculations give a domain wall overlap of 107 nm. From line scans on the MFM data, the width of the overlaps, for the 8 Å and 12 Å samples, are 130 nm and 240 nm, respectively. The excellent quantitative agreement between the calculated and observed domain wall overlap is strong evidence for the model of competing interactions.

## V. TEMPERATURE DEPENDENCE AND OXIDATION/REDUCTION REACTIONS AT THE INTERFACE

The temperature dependence of the IEC consists of an irreversible component arising from chemical changes at the Co/NiO interface and reversible changes arising from a combination of temperature dependences of the magnetic ordering and the anisotropy.

### A. Temperature-induced irreversibility

Heating these samples above room temperature produces a small, permanent decrease in the room temperature minor loop shift (MLS). Figure 10(a) indicates the size of this effect. The data in Fig. 10(a) was taken by increasing the sample temperature (inside an evacuated cryostat) to the value specified on the  $x$  axis. The sample was then allowed to cool in the absence of an external field to room temperature and the MLS was measured. For the strongest AFM coupled sample, with a NiO thickness of 8 Å, the change amounted to 120 Oe after heating the sample to a maximum value of 450 K [Fig. 10(a)].

In order to check for structural changes in the sample with this low-temperature anneal, x-ray reflectivity (XRR), diffraction (XRD), and absorption (XAS) were performed. XRD measurements were performed at the NiO(111) diffraction peak and show that the decrease in the MLS is not due to a structural change in the NiO as there is very little change in either the intensity or the shape of the (111) peak as a function of temperature [Fig. 10(b) inset]. XRR was carried out before and after a 468 K anneal and shows little evidence of a change in the multilayer structure by way of diffusion as there is no decrease in the intensity of the multilayer Bragg peaks and no increase in roughness [Fig. 10(b)]. There is a small change in the Bragg peak position of .12° in  $2\theta$ , indicating a slight change (.45 Å) in the thickness of the Co/Pt multilayers. Previous measurements indicate that annealing even at low temperatures dramatically increases the degree of oxidation/reduction at the interface.<sup>23</sup> Figure 10(c) shows room temperature XAS measurements at the Co  $L_3$  resonance performed before and after [Fig. 10(d)] heating the sample to 450 K. A comparison shows clear evidence of the formation of small amounts of CoO after annealing. This oxidation/reduction reaction occurs at the Co/NiO interface and is responsible for the reduction in the IEC. This result has implications for spin valve structures based on transition metal oxides; even a very small temperature increase from 300 K to 400 K results in an irreversible 40 Oe decrease in

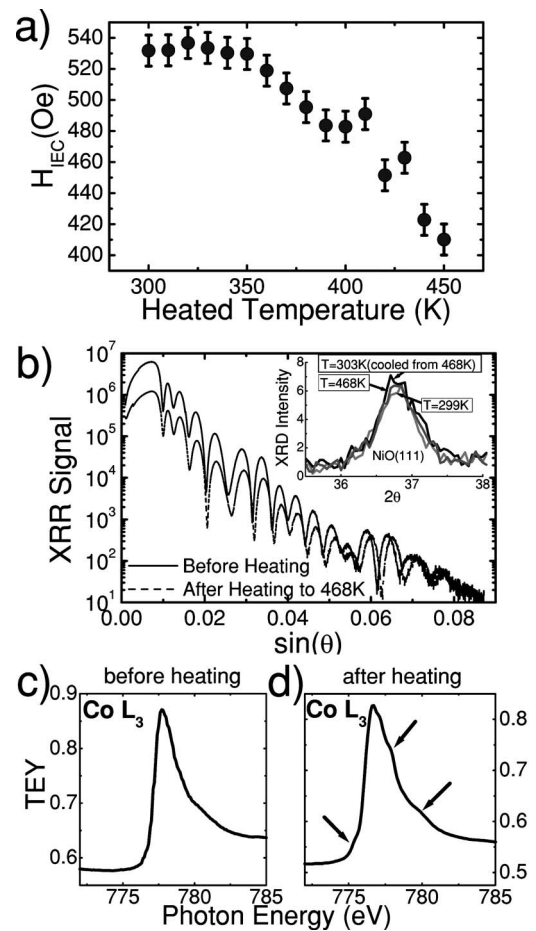


FIG. 10. (a) A plot of the room temperature minor loop shift after heating to a specified temperature, indicated on the horizontal axis. This indicates permanent, irreversible changes in the exchange coupling due to heating, where these changes increase with increased heating. (b) Low-angle x-ray reflectivity taken on an 8 Å sample from series 2 before and after a 468 K heating showing minimal change in the multilayer structure due to diffusion and no evidence of increased roughness. The inset of (b) shows no change in the intensity of the x-ray diffraction at the NiO fcc(111) peak before, at and after a 468 K heating. (c) XAS data taken at the Co  $L_3$  resonance before and after (d) heating to 468 K. The presence of CoO after heating is evident in (d).

the coupling strength. Our data indicate that in addition to roughness and structural inhomogeneities,<sup>35</sup> the details of chemical processes at the interface can be quantitatively correlated with the strength of the magnetic coupling.<sup>22</sup>

### B. Temperature dependence of the minor loop shift

The temperature dependence of the IEC across a spacer layers provides insight into the combination of parameters that govern the coupling. Temperature dependences arise from a combination of spacer layer effects, magnetic layer effects, and the temperature dependence of the reflection coefficients at the interface. Theoretical treatments of the temperature dependence, taking into account some combination of these effects, predict different dependences for metallic and insulating spacer materials.<sup>36-39</sup> For metallic spacer lay-

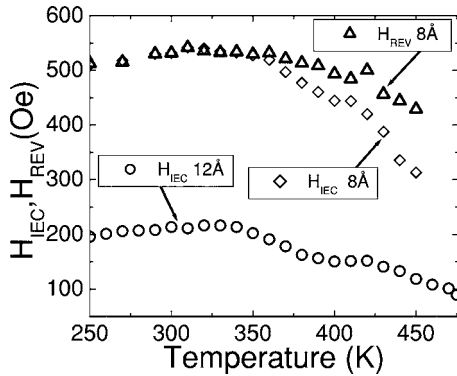


FIG. 11. Interlayer exchange coupling as a function of temperature for the 8 and 12 Å samples, which couple antiferromagnetically. Two plots are given for the 8 Å sample. The  $H_{\text{REV}}$  data are the reversible component of the temperature dependence, obtained as explain in the text. The 8 and 12 Å samples exhibit a decrease in interlayer exchange coupling with increasing temperature.

ers, the smearing of the Fermi surface leads to a reduction in the IEC coupling strength with increasing temperature,<sup>40,41</sup> whereas in an insulating spacer<sup>39</sup> the greater availability of carriers with increasing temperature leads to an increase in the strength of the coupling, an effect seen in  $\text{SiO}_2$  spacer layers<sup>42</sup> and recently in NiO below 350 K.<sup>6,28</sup> The magnetic layer effects are due to magnetic excitations, altering the properties of the magnetic layers. Thermal magnetic disorder may drastically reduce the energy difference between parallel and antiparallel alignment of the magnetic layers and therewith the interlayer coupling.<sup>43</sup>

The effects of temperature on the [Co/Pt]/NiO/[Co/Pt] system are complex and include the temperature dependences of magnetic ordering in both the ferromagnetic [Co/Pt] and the antiferromagnetic NiO, the anisotropy constants and the availability of carriers in the insulating NiO. The data on the temperature dependence of the coupling are shown in Fig. 11. Minor loops were taken *in situ* on samples with a variety of NiO thicknesses in a temperature range of 180 to 470 K using MOKE. We confine our discussion to temperatures above the blocking temperature of 250 K and to AFM coupled samples, since minor loops for the FM coupled samples are harder to ascertain at high temperatures, leading to larger errors in the strength of the IEC. For the strongest AFM coupled samples ( $t_{\text{NiO}}=8$  and 12 Å), the minor loop shift (and thus the coupling) increases slightly and then decreases with temperature. The decrease for the 8 Å sample corresponds to a change of 250 Oe in going from 300 K to 470 K and is significantly larger than the irreversible changes previously discussed (note that all measurements reported here are made on previously unheated samples). Even at the highest temperature of 470 K, the minor loop shift (and hence the IEC) is still present and fairly large. This is consistent with Ref. 28, which indicates that the coupling disappears above 500 K for 11 Å of NiO.

In an attempt to separate the changes in coupling caused by irreversible chemical reactions at the interface from the purely reversible temperature dependence, we have plotted in Fig. 11 the temperature dependence of the IEC coupling for the 8 Å NiO sample (with the strongest AFM coupling)

after accounting for the irreversible changes. Below 300 K,  $\Delta H_{\text{IRR}}$ , the irreversible change in exchange coupling caused by heating the sample, is 0. Above 300 K, we set

$$\Delta H_{\text{REV}}(T) = \Delta H_{\text{IEC}}(T) - \Delta H_{\text{IRR}}(T), \quad (12)$$

where  $\Delta H_{\text{REV}}(T)$  is the change in coupling due to reversible temperature-dependent changes (shown in Fig. 11) and  $\Delta H_{\text{IEC}}(T)$  is the total change measured. There is a slow increase in this purely reversible component of the interlayer coupling from 250 K–300 K followed by a plateau and then a decrease. However, even at the highest temperature of 450 K, the interlayer coupling is large.

Since the AFM ordering of the NiO plays a crucial role in the coupling, we expect the coupling to vanish above the Néel temperature of the NiO. The Néel temperature of a very thin antiferromagnetic film in a FM/AFM/FM trilayer is hard to ascertain experimentally and hence we point to previous experiments. Previous measurements on epitaxial thin films of NiO indicate Néel temperatures of  $\sim 300$  K for a 5 ML sample,<sup>44</sup> a dramatic reduction from the bulk. The presence of a large IEC at temperatures well above this may be explained by the presence of the ferromagnetic Co/Pt, which could stabilize the AFM ordering. Such effects have been seen before. Neutron scattering studies on both  $\text{Fe}_3\text{O}_4/\text{NiO}$  (Ref. 45) and  $\text{Fe}_3\text{O}_4/\text{CoO}$  superlattices<sup>46</sup> show that the ferromagnetic ordering of the  $\text{Fe}_3\text{O}_4$  stabilizes the AFM ordering of the antiferromagnet, leading to Néel temperatures well over the bulk Néel temperature. Hence, it is entirely feasible that the Néel temperature of the NiO in our multilayer sample is enhanced, certainly above the thin film value of 300 K and perhaps even above the bulk value of 525 K. In fact, in many magnetic superlattices, only a single transition temperature (the Curie and/or the Néel temperature) exists for the entire structure.<sup>46,47</sup>

The Curie temperature of the Co/Pt multilayers varies with both Co and Pt thickness, increasing with Co thickness<sup>48</sup> and decreasing with Pt thickness.<sup>49</sup> In samples with thicknesses comparable to ours, the Curie temperature is above 700 K.<sup>47</sup> Recent measurements on similar multilayers indicate that the IEC goes to zero at 526 K,<sup>28</sup> a temperature which is a reasonable candidate for the single transition temperature of the stack. One concern is the effect of the oxidation/reduction reaction at these higher temperatures, an issue that has not been addressed in Ref. 28 and which could conceivably lead to an artificially lowered temperature value for the disappearance of the IEC.

The slight increase in the strength of the IEC over the temperature range 250 K–350 K may be attributed to a steep decrease in the out-of-plane  $K_1$  anisotropy constant with increasing temperature, assuming that the temperature dependence of  $K_1$  is similar to that measured for  $K_2$ .<sup>50</sup> The IEC, which is driven by the Co/NiO interface coupling and mediated through the NiO, depends on both the AFM exchange of the NiO (which tends to align successive spin layers antiparallel) and the anisotropy constant of the NiO [which tends to align the spins in the in-plane (111) direction, minimizing the canting]. In this temperature regime, the anisotropy constant decays rapidly, much faster than the AFM order parameter, leading to a situation whereby the spins

order almost strictly antiparallel to each other, with no frustration at either interface, hence maximizing the coupling. At higher temperatures, the decrease in the antiferromagnetic order parameter reduces the ability of the antiferromagnetic spacer to mediate the coupling, leading to the decrease that is seen.

Our data provide strong evidence for a Néel temperature that is significantly enhanced above the thin film value. In addition, the complex interplay between the various parameters is evidenced in the nonmonotonic temperature dependence.

## VI. CONCLUSIONS

The element specific magnetic behavior measured by XMCD reveals that the in-plane Ni spins in the antiferromagnetic NiO cant out-of-plane and track the out-of-plane Co/Pt magnetization in these oscillatory coupled [Co/Pt]/NiO/[Co/Pt] magnetic heterostructures. XMCD hysteresis loops indicate that the Ni magnetization follows the Co/Pt magnetization as a function of field. On a microscopic level using XMCD PEEM imaging, we have shown that the domains in Co and NiO are exactly coincident, indicating that the tracking of spins occurs domain-by-domain and is not the result of averaging effects. This tracking of spins provides strong support for the model of Zhuravlev *et al.*<sup>16</sup> in which the oscillatory coupling across the NiO spacer layer is simply a result of exchange coupling at the Co/NiO interface and the antiferromagnetic coupling in the NiO layer. In order for this exchange coupling to occur, it is necessary for the Ni spins to cant out-of-plane.

However, a simple relationship between the degree of canting and the strength of the IEC has not been seen. Experimentally, the net Ni out-of-plane magnetization is larger for AFM coupled samples and there is a nonmonotonic dependence of this magnetization on the strength of the coupling. There is strong experimental evidence that the coupling at the upper and lower interfaces differ both in magnitude and sign. We infer that, in common with nearly all magnetic exchange coupling, the microscopic details of the interface structure drive the macroscopic behavior. In this case, we have indirect evidence for differing signs of the coupling at the two interfaces, which may imply different termination layers. Clearly careful structural work is needed in order to see if this is indeed the case.

An unexpected result arising from our work is the extremely short attenuation length for secondary electrons in NiO,  $\sim 4-7$  Å. This has implications for the interpretation of earlier XMCD work,<sup>23</sup> since previous fitting of spectroscopic data assumed a much longer attenuation length based on the universal energy curve. It is possible that other transition metals oxides have similarly short attenuation lengths, quite far removed from the universal energy curve.

Domain imaging using XMCD-PEEM at the Co resonance (which sees only the upper Co/Pt layer due to strong attenuation effects) indicates an increase in the average domain size with increased coupling strength. This is independent of whether the coupling is changed by varying the NiO or Pt thickness and of the sign of the coupling. The IEC acts as an effective anisotropy field, increasing the average size of the domains by making it energetically harder to form domains.

MFM domain images measure both top and bottom Co/Pt layers. Here we once again see clear evidence for domain-by-domain coupling.<sup>7</sup> In addition, in AFM coupled samples, the competition between magnetostatic and IEC leads to a region of domain overlap.<sup>32</sup> This region increases in thickness as the IEC decreases. A simple model giving numerical values for the size of this domain overlap region as a function of coupling strength is found to closely agree with the experimental width obtained from the MFM data.

The temperature dependence of the strength of the IEC shows both irreversible changes (caused by oxidation/reduction reactions at the Co/NiO interface) and reversible changes (which we attribute to the temperature dependences of the myriad factors on which the coupling depends). The most striking feature in the temperature dependence is the fact that the coupling persists at temperatures well above the expected Néel temperature of this thin film of NiO, providing strong evidence for a stabilization of the ordering temperature in the presence of the ferromagnetic Co/Pt.

## ACKNOWLEDGMENTS

The work at the University of Nebraska-Lincoln was supported by NSF (Grants No. MRSEC DMR-0213808 and No. DMR-0203359) and the Nebraska Research Initiative. Use of the Advanced Photon Source was supported by the U.S. Department of Energy, Office of Science, Office of Basic Energy Sciences, under Contract No. W-31-109-ENG-38.

\*Corresponding author: sadenwal@unlserve.unl.edu

<sup>1</sup>B. Dieny, V. S. Speriosu, S. S. P. Parkin, B. A. Gurney, D. R. Wilhoit, and D. Mauri, *Phys. Rev. B* **43**, 1297 (1991).

<sup>2</sup>P. Grünberg, R. Schreiber, Y. Pang, M. B. Brodsky, and H. Sowers, *Phys. Rev. Lett.* **57**, 2442 (1996).

<sup>3</sup>M. N. Baibich, J. M. Broto, A. Fert, F. Nguyen Van Dau, F. Petroff, P. Etienne, G. Creuzet, A. Friederich, and J. Chazelas, *Phys. Rev. Lett.* **61**, 2472 (1988).

<sup>4</sup>E. Popova, J. Faure-Vincent, C. Tiusan, C. Bellouard, H. Fischer, E. Snoeck, M. Hehn, F. Montaigne, V. da Costa, M. Alnot, S.

Andrieu, and A. Schuhl, *Appl. Phys. Lett.* **81**, 509 (2002).

<sup>5</sup>J. Faure-Vincent, C. Tiusan, C. Bellouard, E. Popova, M. Hehn, F. Montaigne, and A. Schuhl, *Phys. Rev. Lett.* **89**, 107206 (2002).

<sup>6</sup>Z. Y. Liu and S. Adenwalla, *Phys. Rev. Lett.* **91**, 037207 (2003).

<sup>7</sup>Z. Y. Liu, L. P. Yue, D. J. Keavney, and S. Adenwalla, *Phys. Rev. B* **70**, 224423 (2004).

<sup>8</sup>J. Unguris, R. J. Celotta, and D. T. Pierce, *Phys. Rev. Lett.* **67**, 140 (1991).

<sup>9</sup>Eric E. Fullerton, K. T. Riggs, C. H. Sowers, S. D. Bader, and A. Berger, *Phys. Rev. Lett.* **75**, 330 (1995).

- <sup>10</sup>S. Adenwalla, G. P. Felcher, Eric E. Fullerton, and S. D. Bader, *Phys. Rev. B* **53**, 2474 (1996).
- <sup>11</sup>J. C. Slonczewski, *J. Magn. Magn. Mater.* **150**, 13 (1995).
- <sup>12</sup>J. Camarero, Y. Pennec, J. Vogel, M. Bonfim, S. Pizzini, F. Ernult, F. Fetta, F. Garcia, F. Lancon, L. Billard, B. Dieny, A. Tagliaferri, and N. B. Brookes, *Phys. Rev. Lett.* **91**, 027201 (2003).
- <sup>13</sup>P. A. A. van der Heijden, C. H. W. Swuste, W. J. M. de Jonge, J. M. Gaines, J. T. W. M. van Eemeren, and K. M. Schep, *Phys. Rev. Lett.* **82**, 1020 (1999).
- <sup>14</sup>M. E. Filipkowski, J. J. Krebs, G. A. Prinz, and C. J. Gutierrez, *Phys. Rev. Lett.* **75**, 1847 (1995).
- <sup>15</sup>Wolfgang Kuch, Liviu I. Chelaru, Francesco Offi, Jing Wang, Masata Kotsugi, and Jurgen Kirschner, *Phys. Rev. Lett.* **92**, 017201 (2004).
- <sup>16</sup>M. Y. Zhuravlev, E. Y. Tsymbal, and S. S. Jaswal, *Phys. Rev. Lett.* **92**, 219703 (2004).
- <sup>17</sup>H. S. Oh and S. K. Joo, *IEEE Trans. Magn.* **32**, 4061 (1996).
- <sup>18</sup>Q. Meng, P. de Haan, W. P. van Drent, J. C. Lodder, and Th. J. A. Popma, *IEEE Trans. Magn.* **32**, 4064 (1996).
- <sup>19</sup>T. K. Hatwar and C. F. Brucker, *IEEE Trans. Magn.* **31**, 3256 (1995).
- <sup>20</sup>J. C. A. Huang, C. H. Lee, and K. L. Yu, *J. Appl. Phys.* **89**, 7059 (2001).
- <sup>21</sup>S. H. Liou and Y. D. Yao, *J. Magn. Magn. Mater.* **190**, 130 (1998).
- <sup>22</sup>H. Ohldag, T. J. Regan, J. Stöhr, A. Scholl, F. Nolting, J. Lüning, C. Stamm, S. Anders, and R. L. White, *Phys. Rev. Lett.* **87**, 247201 (2001).
- <sup>23</sup>T. J. Regan, H. Ohldag, C. Stamm, F. Nolting, J. Lüning, J. Stöhr, and R. L. White, *Phys. Rev. B* **64**, 214422 (2001).
- <sup>24</sup>W. L. O'Brien and B. P. Tonner, *Phys. Rev. B* **50**, 12672 (1994).
- <sup>25</sup>Reiko Nakajima, J. Stöhr, and Y. U. Idzerda, *Phys. Rev. B* **59**, 6421 (1999).
- <sup>26</sup>X-ray attenuation data can be found at [http://www.cxro.lbl.gov/optical\\_constants/atten2.html](http://www.cxro.lbl.gov/optical_constants/atten2.html)
- <sup>27</sup>M. P. Seah and W. A. Dench, *Surf. Interface Anal.* **1**, 2 (1979).
- <sup>28</sup>Z. Y. Liu, G. H. Yu, and Z. C. Wang, *Phys. Rev. B* **72**, 064451 (2005).
- <sup>29</sup>D. L. Abraham and H. Hopster, *Phys. Rev. Lett.* **58**, 1352 (1987).
- <sup>30</sup>M. T. Hutchings and E. J. Samuelsen, *Phys. Rev. B* **6**, 3447 (1972).
- <sup>31</sup><http://rsb.info.nih.gov/ij/>
- <sup>32</sup>Olav Hellwig, Andreas Berger, and Eric E. Fullerton, *Phys. Rev. Lett.* **91**, 197203 (2003).
- <sup>33</sup>E. Y. Tsymbal, *Appl. Phys. Lett.* **77**, 2740 (2000).
- <sup>34</sup>E. Y. Tsymbal, *J. Magn. Magn. Mater.* **130**, L6–L12 (1994).
- <sup>35</sup>J. Nogués, D. Lederman, T. J. Moran, Ivan K. Shuller, and K. V. Rao, *Appl. Phys. Lett.* **68**, 3186 (1996).
- <sup>36</sup>S. Schwieger and W. Nolting *Phys. Rev. B* **69**, 224413 (2004).
- <sup>37</sup>P. Bruno and C. Chappert, *Phys. Rev. Lett.* **67**, 1602 (1991).
- <sup>38</sup>D. M. Edwards, J. Mathon, R. B. Muniz, and M. S. Phan, *Phys. Rev. Lett.* **67**, 493 (1991).
- <sup>39</sup>P. Bruno, *Phys. Rev. B* **52**, 411 (1994).
- <sup>40</sup>Z. Zhang, L. Zhou, P. E. Wigen, and K. Ounadjela, *Phys. Rev. Lett.* **73**, 336 (1994).
- <sup>41</sup>N. Persat and A. Dinia, *Phys. Rev. B* **56**, 2676 (1997).
- <sup>42</sup>B. Briner and M. Landolt, *Europhys. Lett.* **28**, 65 (1994).
- <sup>43</sup>S. Schwieger, J. Kienert, and W. Nolting, *Phys. Rev. B* **71**, 174441 (2005).
- <sup>44</sup>D. Alders, L. H. Tjeng, F. C. Voogt, T. Hibma, G. A. Sawatzky, C. T. Chen, J. Vogel, M. Sacchi, and S. Iacobucci, *Phys. Rev. B* **57**, 11623 (1998).
- <sup>45</sup>J. A. Borchers, R. W. Erwin, S. D. Berry, D. M. Lind, J. F. Ankner, E. Lochner, K. A. Shaw, and D. Hilton, *Phys. Rev. B* **51**, 8276 (1995).
- <sup>46</sup>P. J. van der Zaag, Y. Ijiri, J. A. Borchers, L. F. Feiner, R. M. Wolf, J. M. Gaines, R. W. Erwin, and M. A. Verheijen, *Phys. Rev. Lett.* **84**, 6102 (2000).
- <sup>47</sup>Ken Takano, Ph.D. thesis, University of California-San Diego, 1998.
- <sup>48</sup>Junsaku Nakajima, Akira Takahashi, Kenji Ohta, and Toshio Ishikawa, *J. Appl. Phys.* **73**, 7612 (1993).
- <sup>49</sup>S. Hashimoto, *J. Appl. Phys.* **75**, 438 (1994).
- <sup>50</sup>K. Kurosawa, M. Miurat, and S. Saito, *J. Phys. C* **13**, 1521 (1980).